Science Advances
AAAS

advances.sciencemag.org/cgi/content/full/6/25/eabb1327/DC1

Supplementary Materials for

Programming van der Waals interactions with complex symmetries into microparticles using liquid crystallinity

H. A. Fuster, Xin Wang, Xiaoguang Wang, E. Bukusoglu, S. E. Spagnolie, N. L. Abbott*

*Corresponding author. Email: nabbott@cornell.edu

Published 19 June 2020, *Sci. Adv.* **6**, eabb1327 (2020)
DOI: 10.1126/sciadv.abb1327

This PDF file includes:

Figs. S1 to S9
Table S1
References

Supplementary Materials

Microparticle Imaging

As described in the main text (Figure 1E and associated text), we characterized the adsorption of thousands of probe colloids onto hundreds of polymerized microparticles to obtain the surface adsorption statistics reported in this paper. To determine the location of PS colloids adsorbed onto the surfaces of LC microparticles, videos of the LC microparticles (fluorescence imaging) were recorded while varying the location of the focal plane in the z-direction. We determined the image frame in which each PS colloid was in focus (as evidenced by a maximal light intensity relative to its background) and assigned the z-location of the colloid to that frame. This procedure was repeated to ensure that the PS colloids were immobile on the surface of the LC microparticles. Figure S1 shows representative fluorescence micrographs taken from these videos, documenting probe colloids adsorbed to polymerized bipolar and radial LC microparticles.

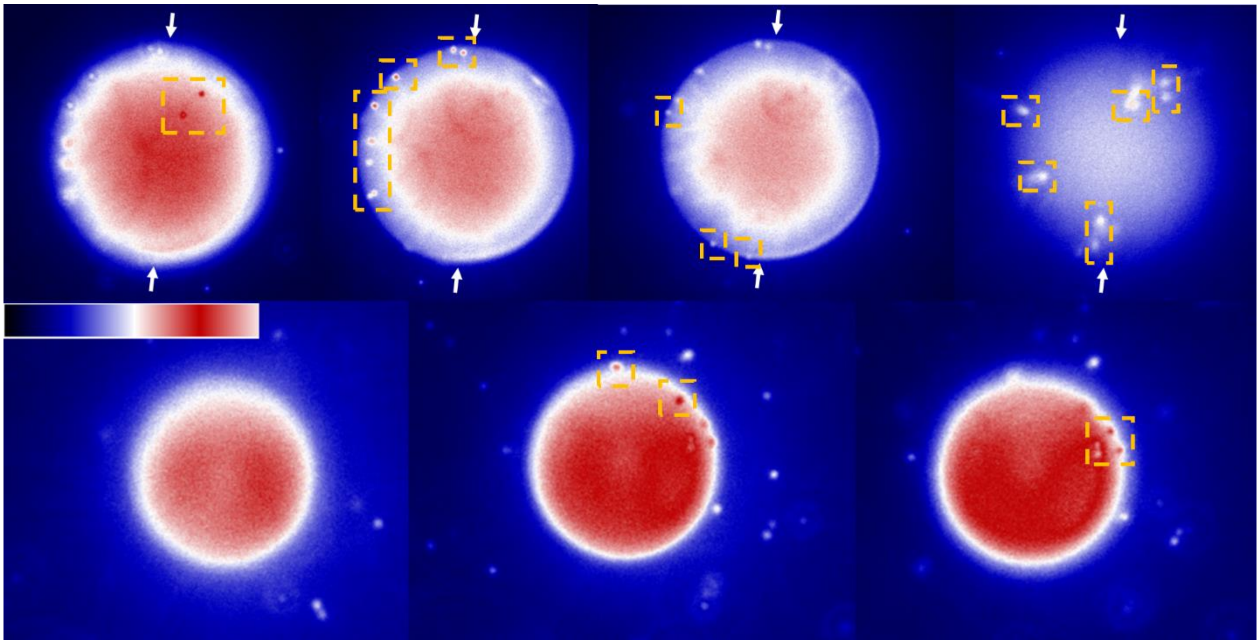

Figure S1. Fluorescence microscopy characterization of microparticles. Colorized fluorescence micrographs of bipolar (top row) and radial (bottom row) microparticles with adsorbed probe colloids. The rows of images were obtained by moving the focal plane of the microscope in the z-direction. White arrows indicate the location of the surface defects on the bipolar microparticle. Orange boxes indicate the location of probe colloids as they come into focus in the image plane. The bipolar microparticle is 38 μm in diameter and the radial microparticle is 28 μm in diameter. (Inset) LUT for the color shift (ImageJ, ‘UnionJack’).

Change in Fluorescence Intensity of LC Microparticles with Time

During imaging of LC microparticles following addition of probe PS colloids, we observed the fluorescence intensity of the LC microparticles to change with time. To compensate for this change, the exposure times were adjusted during measurements to enable visualization of the PS probe colloids as shown in Figure 1. To illustrate this point, we show additional results, similar to those in Figure 1D, but with imaging performed at constant exposure time. Bipolar and radial LC microparticles were mixed with PS colloids in water with no added salts and fluorescence micrographs were obtained over 30 minutes (Figure S2). Inspection of Figure S2 revealed that the fluorescence intensity of the microparticles increased with time. In both cases, there was no adsorption of PS colloids on the surfaces of the microparticles. We hypothesize that the hydrophobic dye with which the PS colloids are impregnated is partially soluble in water, leading to a net flux of the dye from the PS colloids into the LC microparticles. The observation of time-dependent fluorescence does not impact any of the conclusions reported in this paper.

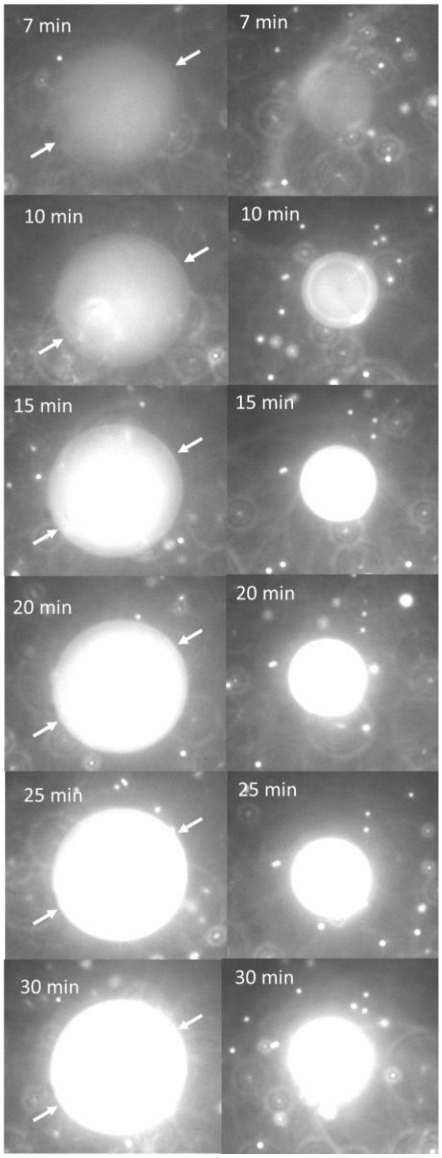

Figure S2. Observation of changes in microparticle fluorescence with time. Fluorescence micrographs showing the change in fluorescence intensity of a bipolar (left column) and radial (right column) LC microparticle with time following addition of fluorescent probe colloids (at constant exposure time). White single-headed arrows show the locations of surface defects for bipolar LC microparticles. Time after addition of PS probe colloids is shown in the top left corner of each micrograph. The bipolar LC microparticle is 40 μm in diameter and the exposure time is 10 ms. The radial LC microparticle is 22 μm in diameter and the exposure time is 60 ms.

Van der Waals Interactions with LC Slabs

As a first step towards understanding how the local orientation of a LC can change the strength of van der Waals interactions with a probe PS colloid in water, we calculated the Hamaker constant, A_{132}, for a LC slab with either planar (or parallel) surface anchoring or homeotropic (or perpendicular) surface anchoring (Figures S3A and S3B) as

$$A_{132} \approx \frac{3}{4} k_B T \left(\frac{\varepsilon_1 - \varepsilon_3}{\varepsilon_1 + \varepsilon_3}\right)\left(\frac{\varepsilon_2 - \varepsilon_3}{\varepsilon_2 + \varepsilon_3}\right) + \frac{3hv_e}{8\sqrt{2}} \frac{(n_1^2 - n_3^2)(n_2^2 - n_3^2)}{(n_1^2 + n_3^2)^{1/2}(n_2^2 + n_3^2)^{1/2}[(n_1^2 + n_3^2)^{1/2} + (n_2^2 + n_3^2)^{1/2}]} \qquad \text{(S1)}$$

where T is the temperature, k_B is the Boltzmann constant, ε_j is the relative dielectric permittivity of phase j, n_j is index of refraction of the phase, h is the Planck constant, and v_e is a characteristic absorption frequency of light for the interacting phases (1). In Eq. S1, phase 1 is PS, phase 2 is LC, and phase 3 is water. The influence of the LC orientation on van der Waals interactions is evaluated in Eq. S1 by using ordinary and extraordinary optical properties of 5CB (33, 34) as shown in Table S1.

We calculated the Hamaker constant corresponding to planar and homeotropic surface anchoring to be 1.7 x 10^{-20} J and 1.3 x 10^{-20} J, respectively (Figure S3C). A PS probe colloid approaching a slab of LC at a surface-to-surface separation, s, in an aqueous salt solution will experience an attractive interaction that depends on LC ordering (Figure S3D). For example, a PS probe colloid (radius, R, = 0.5 μm) in a 6 mM NaCl solution (Debye screening length, κ = 3.92 nm) approaching a LC slab at a separation of 5 nm would experience an attractive van der Waals interaction energy ($\phi_{Attract} = -AR/6s$) of -53.3 k_BT and -68.3 k_BT when the LC ordering is perpendicular and planar to the interface, respectively. By assuming that (i) the repulsive electrical double layer interactions for the two LC slabs are identical, (ii) water has a dielectric constant of ε_r = 78.54, (iii) constant surface charge density, and (iv) the surface potentials at infinite separation of the LC and PS are both ψ_0 = -50 mV, we subsequently calculate the repulsive electrical double layer interaction ($\phi_{Repel} = \varepsilon_r \varepsilon_0 R \psi_0^2/2\,[\ln((1+e^{-\kappa s})/(1-e^{-\kappa s})) - \ln(1-e^{-2\kappa s})]$), asymptotic solution to an expression given by (*41*)) to be 60.3 k_BT. This result indicates that there is a net repulsion (net positive interaction energy) between the PS probe colloid and LC slab with perpendicular LC ordering whereas a net attraction (net negative interaction energy) is predicted for a PS probe colloid and LC slab with parallel LC ordering.

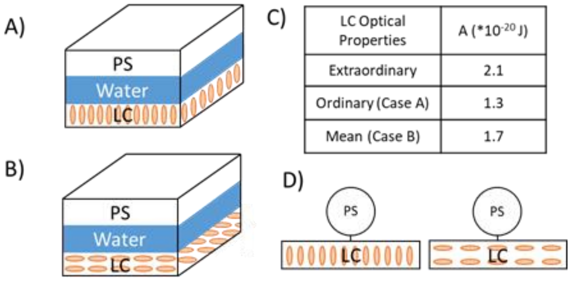

LC Optical Properties	A (*10^{-20} J)
Extraordinary	2.1
Ordinary (Case A)	1.3
Mean (Case B)	1.7

Figure S3. Predictions of van der Waals interactions for a slab geometry. PS (phase 1) interacts across water (phase 3) with homeotropic (**A**) and planar (**B**) LC (phase 2). (**C**) The Hamaker constants calculated according to Equation S1. (**D**) PS colloid near a slab of LC.

Table S1. Optical and dielectric properties used in the calculation of Hamaker constants. We report the following optical and dielectric properties for the LCs used in our system: 5CB; n_e = 1.71, n_o = 1.53; ε_e = 18.4, ε_o = 6.8 at 25 °C (*42*, *43*) and RM257; n_e = 1.69, n_o = 1.51, $\Delta\varepsilon$ = -1.8 at 25 °C (*44*, *45*)).

	Phase 1 (PS)	Phase 3 (Water)	Phase 2 Properties	Phase 2 (LC)
Relative dielectric constant, ε	2.6	78	Extraordinary	18.4
			Ordinary	6.8
Index of Refraction, *n*	1.6	1.33	Extraordinary	1.71
			Ordinary	1.53

Calculation of LC Microparticle Director Profiles

I. Energetics and Equilibrium Equations

First, we considered the elastic free energy density written in terms of derivatives of a local nematic director field $\hat{n}$:

$$W(\hat{n}) = \frac{K_1}{2}(\nabla \cdot \hat{n})^2 + \frac{K_2}{2}(\hat{n} \cdot \nabla \times \hat{n})^2 + \frac{K_3}{2}|\hat{n} \times (\nabla \times \hat{n})|^2 \tag{S2}$$

where K_1, K_2, and K_3 are the elastic constants for the splay, twist, and bend modes of LC, respectively. The elastic energy was evaluated as $\varepsilon = \int_\Omega W dx$, where x ∈ Ω, a spherical domain centered at the origin of radius a. To find the equilibrium configuration, we minimized ε subject to the constraint $|\hat{n}| = 1$, leading to **h** = 0, where **h** is the molecular field, $h = H - \hat{n}\hat{n} \cdot H$, with $H = -\delta W/\delta\hat{n}$.

We assumed that no twist was present in our system. We described the director field as $\hat{n} = \sin\theta(x)(\cos\chi\hat{x} + \sin\chi\hat{y}) + \cos\theta(x)\hat{z}$. We performed calculations using a spherical coordinate system with r ∈ [0, a], $\eta = \tan^{-1}(\frac{z}{\sqrt{x^2+y^2}})$ as the polar angle measured from the positive z axis, and χ as the azimuthal angle. We parametrized the domain Ω by $x(r,\eta,\chi) = r[\sin\eta\,(\cos\chi\hat{x} + \sin\chi\hat{y}) + \cos\theta(x)\hat{z}]$. For the bipolar microparticle system, which has a cylindrically symmetric director configuration, we described θ as $\theta = \theta(r,\eta)$ and the director field as

$$\hat{n} = \sin\theta(r,\eta)\,[\cos(\chi)\,\hat{x} + \sin(\chi)\,\hat{y}] + \cos\theta(r,\eta)\hat{z}]. \tag{S3}$$

To account for energetic penalties associated with a departure from tangential anchoring along the boundary, $\delta\Omega$, we added a surface energy to the energy functional. For degenerate tangential anchoring, we included the penalty

$$W_S = \frac{W}{2}\int_{\delta\Omega}(\hat{n} \cdot \hat{r})^2 dS = \pi a^2 W \int_0^\pi \cos(\eta - \theta(a,\eta))^2 \sin\eta\, d\eta. \tag{S4a}$$

We note that if the director field is *nearly* tangential to the surface, $\theta(a,\eta) \approx \eta + \pi/2$ and then $W_S \approx \pi a^2 \int_0^\pi (\theta(a,\eta) - \left[\eta + \frac{\pi}{2}\right])^2 \sin\eta\, d\eta$.

To account for energetic penalties associated with departure from homeotropic anchoring along the boundary, $\delta\Omega$, we instead added the surface energetic penalty

$$W_S = \frac{W}{2}\int_{\delta\Omega}[1-(\hat{n}\cdot\hat{r})^2]dS = \pi a^2 W\int_0^\pi \sin(\eta-\theta(a,\eta))^2\sin\eta\,d\eta. \qquad \text{(S4b)}$$

II. PDES and Boundary Conditions

To find the governing equations for $\theta(r,\eta)$, and boundary conditions, we minimized the total energy. We used the single constant approximation (*46*), $K_1 = K_2 = K_3 = K$, and assumed degenerate planar anchoring conditions. By letting $\theta \to \theta + \varepsilon f$ and by computing the first derivative of the total energy with respect to ε (the first variational derivative), we found (integrating in χ)

$$\delta\varepsilon = 2\pi\int_0^\pi\int_0^a \{A_0 f + A_1 f_r + A_0 f_\eta\}\,dr\,d\eta + 2\pi\int_0^\pi A_w f(a,\eta)d\eta, \qquad \text{(S5)}$$

$$A_0(r,\eta) = \frac{1}{4}\sin\eta\sin(2\theta)\,(1-\cot^2(\eta)),$$

$$A_1(r,\eta) = r^2\sin\eta\theta_r\,, A_2(r,\eta) = \sin\eta\theta_\eta,$$

$$A_w = a^2 W\sin\eta\,\{[\sin\eta\cos\theta\cos\chi - \cos\eta\sin\theta][\sin\eta\sin\theta\cos\chi + \cos\eta\cos\theta]\}_{r=a}$$

where the metric terms $r^2\sin\eta$ and $a^2\sin\eta$ have been bundled into the definitions above. Given the axisymmetry of the system, we applied the boundary condition $\theta(r,\eta=0)=0$ and either $\theta(r,\eta=\pi)=0$ or $\theta(r,\eta=\pi)=\pi$. We assumed variations with $f(r,0)=f(r,\pi)=0$, and $f(0,\eta)=0$. By integrating by parts, we found coupled equations satisfied by θ and φ at equilibrium,

$$A_0 - \partial_r A_1 - \partial_\eta A_2 = 0, \{r\in[0,a], \eta\in[0,\pi]\}, \qquad \text{(S6)}$$

along with the boundary conditions,

$$A_w(\eta) + A_1(a,\eta) = 0, \eta\in[0,\pi].$$

By rewriting the above in terms of θ, we found

$$r^2\nabla^2\theta + \frac{1}{4}(\cos(2\eta) - 2)\csc^2\eta\,\sin(2\theta) = 0, \tag{S7}$$

where $\nabla^2 = \delta_{rr} + 2r^{-1}\delta_r + r^{-2}[\cot(\eta)\,\delta_\eta + \delta_{\eta\eta}]$. For tangential anchoring, we obtained the following boundary conditions

$$\theta(0,\eta) = \theta(r,0) = \theta(r,\pi) = 0,$$

$$2K\theta_r(a,\eta) + W\sin\Big(2\big(\eta - \theta(a,\eta)\big)\Big) = 0, \eta \in [0,\pi].$$

These equations were discretized using second-order finite differences with mixed boundary conditions incorporated at the boundaries using ghost points. A special treatment at the coordinate singularity at $r = 0$ was used to preserve second-order accuracy

$$\theta(r = 0,\eta) = 2\langle\theta(r = \Delta r,\eta)\rangle - \langle\theta(r = 2\Delta r,\eta)\rangle. \tag{S8}$$

Convergence tests returned the expected decay of the error with increasing spatial resolution. In the remainder of the work below, we used $N_r = 256$ radial gridpoints and $N_\eta = 64$ polar angle gridpoints. The equations were solved in dimensionless units, $r \in [0,1]$ and $\eta \in [0,\pi]$, and we scaled the results by the length a for presentation purposes.

A. Homeotropic Anchoring

In addition to treating the boundary conditions at the LC surface as described above, we directly inserted a point along the z-axis where the director field experienced a singularity to produce radial and pre-radial homeotropic configurations. Writing this point as z*, we included the boundary conditions

$$\theta(r > z^*,\eta = 0) = 0, \tag{S9}$$

$$\theta(0 < r \leq z^*,\eta = 0) = \pi,$$

$$\theta(0 \leq r \leq a,\eta = \pi) = \pi.$$

III. Numerical Solution

To solve the equations above for general anchoring strength, we described the system as

$$A\theta = N(\theta) \tag{S10}$$

where θ was a column vector representing the entire field $\theta(r,\eta)$, and A was the linear operator which included parts of the boundary conditions. This operator only needed to be formed once, and was stored (and inverted) as a sparse matrix. $N(\theta)$ contained all the nonlinear portions of the equation above. We solved the following vector equation,

$$F(\theta) = \theta - A^{-1}\big(N(\theta)\big) = 0. \tag{S11}$$

by applying Newton iteration with automated Jacobian updating (Broyden's method),

$$\theta_{n+1} = \theta_n - J_n^{-1}F(\theta_n), \tag{S12}$$

$$J_n = \frac{\partial F}{\partial \theta}(\theta_n) = I - A^{-1}G_n,$$

$$G_n = \frac{\partial N}{\partial \theta}(\theta_n).$$

This was accomplished by finite difference approximation at the first iterative step; for the remaining steps we updated the Jacobian inverse as:

$$J_{n+1}^{-1} = J_n^{-1} + \frac{\Delta\theta_n - J_n^{-1}\Delta F(\theta_n)}{\Delta\theta_n^T J_n^{-1}\Delta F(\theta_n)}\Delta\theta_n^T J_n^{-1}, \tag{S13}$$

where $\Delta\theta_n = \theta_n - \theta_{n-1}$ and $\Delta F_n = F(\theta_n) - F(\theta_{n-1})$. In addition, we first solved the system using linearized boundary conditions, and used this solution as the seed for solving the full nonlinear system above. Selected director fields found are shown for dimensionless tangential anchoring strengths $w = aW/K$ in Figure S4. Cross sections of the radial and pre-radial configurations (with strong homeotropic anchoring) are also shown in Figure S4.

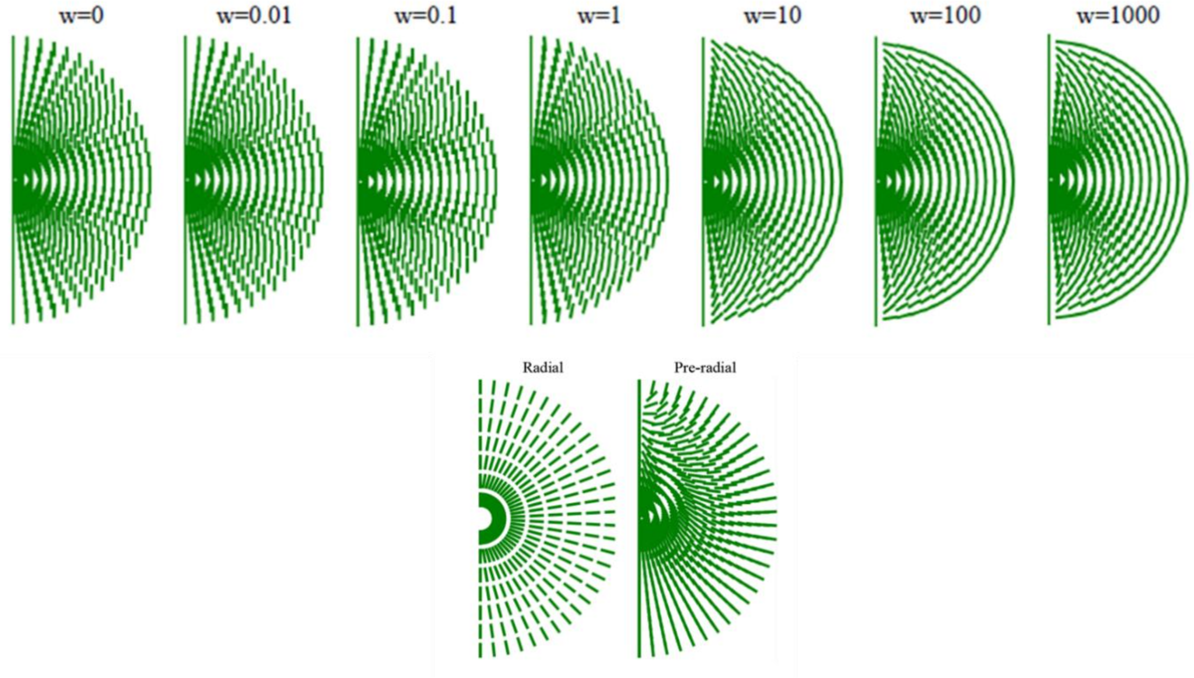

Figure S4. Calculated director configurations for LC microparticles at varying anchoring energies. (Top row) Calculated cross-sections of the director field of LC microparticle with tangential anchoring conditions and dimensionless anchoring strengths $w = aW/K$. (Bottom row) Calculated cross-sections of the radial and preradial director configurations of LC microparticles with strong (w = 1000) homeotropic anchoring conditions.

Calculation of van der Waals Interaction Energy

We calculated van der Waals interaction energies by summing interactions of the probe colloid with constituent volumes of polymerized LC within the microparticles. The interaction energy evaluated by Hamaker is represented by the double integral (*41*, *47*)

$$\phi_{Attract} = \int_{\Omega_1}\int_{\Omega_2} \frac{-A}{2\pi^2}\frac{1}{|x_1 - x_2|^6}\, dV_1 dV_2 \tag{S14}$$

where Ω_1 and Ω_2 are spherical volumes and x_1 and x_2 are the center positions of the two interacting volumes (i.e., the volume elements of LC microparticle and probe colloid, respectively). The Hamaker constant, *A*, of Eq. S14 changes with the orientation of LC within the interacting LC microparticle volume elements. Near the interface of a bipolar microparticle, these volume elements have a near-homeotropic orientation close to the surface defect (relative to the interface) and near-planar orientation close to the equatorial region (relative to the interface). We evaluated the Hamaker constant describing the interaction of the probe colloid with the local volume element of polymerized LC as

$$A(\alpha) = (A_m - A_o)\sin(\alpha) + A_o \tag{S15}$$

where α is the angle between the local nematic director and the centerline between x_1 and x_2, evaluated as $\cos(\alpha) = |(x_2 - x_1)\cdot n(x_1)|/|x_2 - x_1|$, using absolute values to restrict alpha to positive values and angles from 0° to 90°, and A_m and A_o are the Hamaker constants as calculated using the arithmetic mean of the ordinary and extraordinary refractive indices and dielectric constants and ordinary refractive index and dielectric constant of the LC as shown in Figure S3C, respectively. Substituting Eq. S15 for the Hamaker constant, *A*, in Eq. S14 resulted in

$$\phi_{Attract} = \frac{-1}{2\pi^2}\int_{\Omega_1}\int_{\Omega_2} \frac{A_o + (A_m - A_o)\sin(\alpha)}{|x_1 - x_2|^6}\, dV_1 dV_2 \tag{S16}$$

After integration of Eq. S16 over the probe colloid, Ω_2, the interaction energy between an infinitesimal volume of the LC microparticle, Ω_1, of vanishing radius b, was given by Taylor expansion of Eq. S14 about small b:

$$\phi_b(x_1) = \frac{-4{r_1}^3[A_o + (A_m - A_o)\sin(\alpha)]}{3\pi(R(x_1)^2 - {r_1}^2)^3}\left(\frac{4\pi b^3}{3}\right) \tag{S17}$$

where R(x_1) is the distance between the probe colloid center and the volume element of LC. These interaction energy contributions were summed, after scaling the above by dV_1/(4πb^3/3), resulting in an integral that required numerical integration:

$$\phi_{Attract} = \int_{\Omega_1} \phi_b(x_1)\frac{dV_1}{4\pi b^3/3} = \frac{-4{r_1}^3}{3\pi}\int_{\Omega_1} \frac{[A_o + (A_m - A_o)\sin(\alpha)]}{(R(x_1)^2 - {r_1}^2)^3} dV_1 \tag{S18}$$

The integration of Equation S18 was non-trivial to compute accurately. We used adaptive quadrature with relative and absolute error tolerances of 10^{-5}, and an interpolation of the director field to evaluate arbitrary points in space.

To verify the accuracy of the numerical integration of Eq. S18, we began by performing the integration with A_m = 0 (i.e., an isotropic microparticle). We compared the results of the numerical integration of Eq. S18 to the analytical solution of Eq. S14 when applied to an isotropic microparticle (*1*, *41*), namely

$$\phi_{Attract} = -\frac{A}{6}\left[\frac{2r_1r_2}{f_1} + \frac{2r_1r_2}{f_2} + \ln\left(\frac{f_1}{f_2}\right)\right] \tag{S19}$$

$$f_1 = s^2 + 2sr_1 + 2sr_2$$

$$f_2 = s^2 + 2sr_1 + 2sr_2 + 4r_1r_2$$

where s is the surface-to-surface separation, r_1 is the LC microparticle radius, and r_2 is the PS probe colloid radius. Figure S5a shows the scaled interaction energy using A_o = 3.2 k$_B$T, A_m = 0, a microparticle radius of 10 μm, a probe colloid radius of 0.5 μm, for a range of distances and α between the probe colloid and microparticle. Inspection of Figure S5a reveals good agreement between the numerical expression evaluated using Eq. S18 and the analytical expression evaluated using Eq. S19.

Next, we investigated the impact of liquid crystallinity (i.e., non-zero A_m) on the van der Waals interaction energy. Using the energetically minimized director profiles calculated for bipolar microparticles for varying anchoring strengths (assuming a single LC elastic constant, K = 6.6 pN), we numerically evaluated Eq. S18 to obtain ‘exact’ van der Waals interaction energies (dashed lines, Figure S5b and S5c). Inspection of Figure S5b and S5c reveals that the introduction of liquid crystallinity (A_m = 0.9 k_BT) causes spatial variation in the magnitude of the attractive interaction energies calculated for an intermediate (W = 6.2 μN/m) and a strong (W = 64.5 μN/m) tangential surface anchoring, respectively.

These calculations were computationally costly and thus an approximation was explored to speed calculations for bipolar microparticles. We shrank the size of Ω_1 in Eq. S18 to incorporate only those LC volume elements of the microparticle closest to the probe colloid, and again calculated the resulting van der Waals interaction energy as a function of tangential anchoring energy and angle, α (solid lines, Figure S5b and S5c). Inspection of Figure S5b and S5c reveal that for both strong and intermediate tangential anchoring energies, evaluation of van der Waals interactions between the bipolar microparticle and PS colloid based on the surface LC volume elements introduces minimal (<5%) error.

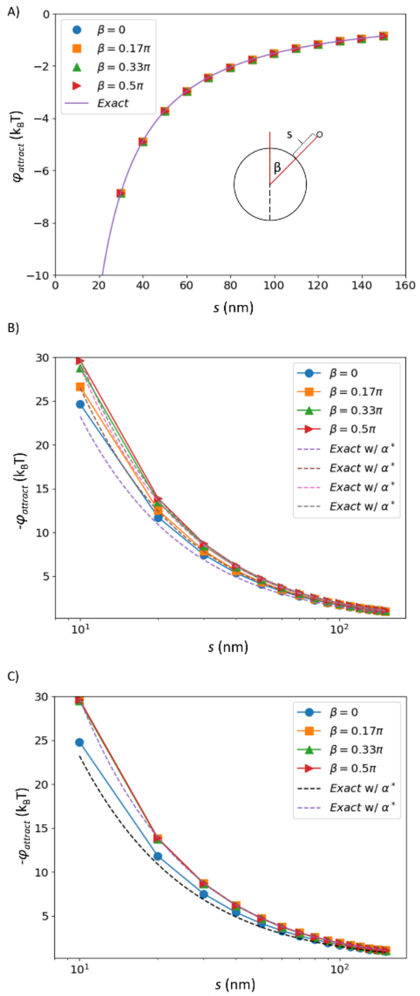

Figure S5. Comparison of calculations of the van der Waals interaction energies. Scaled interaction energies using A_o = 3.2 k_BT, LC microparticle radius a = 10 µm, and probe colloid radius of 0.5 µm. (**A**) When A_m = 0 (i.e., the microparticle is isotropic), the net interaction energy as a function of surface-to-surface separation, s, over a range of angles of incidence, β, evaluated using expressions Eq. S18 and Eq. S19. (Inset) Illustration demonstrating the geometry of the interacting microparticle and probe colloid. The axis of symmetry is the dashed line. (**B**, **C**) Evaluation of Eq. S18 with A_m = 0.9 k_BT, K = 6.6 pN and intermediate (W = 6.2 µN/m, **B**) and strong (W = 64.5 µN/m, **C**) tangential surface anchoring using near-surface LC volume elements (solid lines) and complete set of LC elements defining the microparticle volume (dashed lines).

Evaluation of Net Interaction Energies

As outlined in the previous section of the Supplementary Materials, the van der Waals interaction energy of a probe colloid with an LC microparticle can be evaluated by using an effective Hamaker constant that varies with position around the LC microparticle. The net interaction energy was then calculated by summing Eq. S19 with (*1*, *41*)

$$\phi_{Repel} = \frac{\varepsilon r_1 r_2 \left(\psi_{0,1}^2 + \psi_{0,2}^2\right)}{4(r_1 + r_2)} \left[\frac{2\psi_{0,1}\psi_{0,2}}{\psi_{0,1}^2 + \psi_{0,2}^2} \ln\left(\frac{1 + e^{-\kappa s}}{1 - e^{-\kappa s}}\right) - \ln(1 - e^{-2\kappa s})\right] \qquad \text{(S20)}$$

where ε is the absolute dielectric permittivity, $\psi_{0,1}$ and $\psi_{0,2}$ are the surface potentials of the LC microparticle and probe colloid at infinite separation, respectively, and κ^{-1} is the Debye screening length. We note that Eq. S20 assumes a constant surface charge density as a function of the separation of the probe colloid and LC microparticle *(25, 41)*. Interaction energies calculated according to these equations are presented in Figures 4A and 4B.

Determination of the Surface Potentials

We measured the zeta potentials of the LC microparticles to be approximately -50 mV, which we interpret as a lower bound to the surface potentials at infinite separation (*48*). An upper bound to the surface potentials at infinite separation is approximately -80 mV, which is the point when charge-determining ions in water saturate the surfaces of organic oils in aqueous dispersions (*49*, *50*). Accordingly, we examined predictions of our model for $\psi_{0,1} = \psi_{0,2} = -40$ mV, -50 mV, and -60 mV. Examination of Figure S6A and S6B reveals that at a surface potential at infinite separation of -40 mV, the probe colloid experiences van der Waals interaction energies that exceed the repulsive electrical double layer interaction energy both at the equator and pole of the bipolar microparticle. Conversely, at a surface potential at infinite separation of -60 mV, the probe colloid experiences repulsive electrical double layer interaction energy in excess of attractive van der Waals interaction energy above both the equator and pole of the bipolar microparticle. At a surface potential at infinite separation of -50 mV, above the equator of the bipolar microparticle, the van der Waals attractions are stronger than electrical double layer repulsions, whereas above the pole of the LC microparticle the electrical double layer repulsions generates an energy barrier to aggregation of the probe colloid and LC microparticle. It is this latter behavior that matches with our experimental observations and led us to use a surface potential at infinite separation of -50 mV in our calculations.

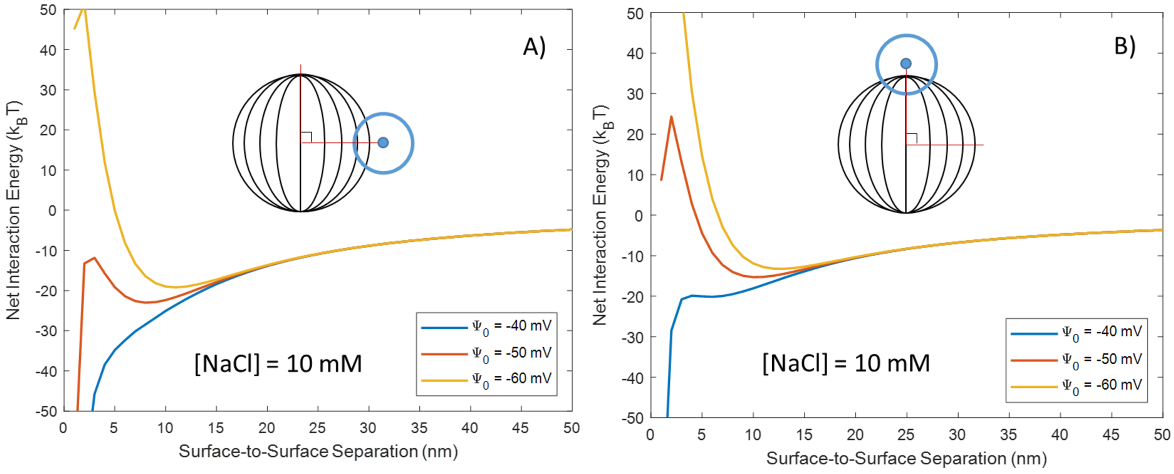

Figure S6. Calculation of net interaction energies at varying surface potentials. Calculated net interaction energies as a function of surface-to-surface separation for PS probe colloids located either at the equatorial region (**A**) or polar region (**B**) of a bipolar LC microparticle. Results are shown for different symmetric surface potentials with 10 mM NaCl (Debye screening length = 3.04 nm) and an intermediate tangential surface anchoring energy (W = 6.2 µN/m).

Calculation of Probe Colloid Flux onto Microparticle Surfaces

Eq.2 of the main text shows the flux expression with hydrodynamic effects calculated as (*28*, *29*)

$$\frac{D_{12}^{\infty}}{D_{12}}(\rho) = 1 + \frac{2.6 r_1 r_2}{(r_1+r_2)^2}\sqrt{\frac{r_1 r_2}{(r_1+r_2)(\rho r_1 - r_1 - r_2)}} + \frac{r_1 r_2}{(r_1+r_2)(\rho r_1 - r_1 + r_2)}. \qquad \text{(S21)}$$

The variables are defined in Eq. 2.

The corrected flux, J_C, calculated according to Eq. 2 at a given surface anchoring energy, was integrated with respect to angle of incidence, β, over the surface regions defined in Figures 1F and 5D. These values were then normalized by the flux evaluated at a reference surface region (polar region VI for the bipolar microparticle, or equatorial region III for the preradial microparticle).

$$\text{Surface Density} = \frac{\int_0^{2\pi}\int_x^y J_C(\beta) {r_1}^2 \sin(\beta)\, d\beta d\chi}{\int_0^{2\pi}\int_x^y {r_1}^2 \sin(\beta)\, d\beta d\chi} = \frac{\int_x^y J_C(\beta)\sin(\beta)\, d\beta}{\int_x^y \sin(\beta)\, d\beta} \qquad \text{(S22)}$$

$$\text{Normalized Surface Density} = \frac{\dfrac{\int_x^y J_C(\beta)\sin(\beta)\, d\beta}{\int_x^y \sin(\beta)\, d\beta}}{\dfrac{\int_0^{\pi/6} J_C(\beta)\sin(\beta)\, d\beta}{\int_0^{\pi/6} \sin(\beta)\, d\beta}}$$

where x and y define regions on the surface of the microparticle (0 to π/6 for regions I and VI, π/6 to π/3 for regions II and V, and π/3 to π/2 for regions III and IV).

Calculation of van der Waals Interaction Energy and Probe Colloid Flux for Pinned Preradial LC Microparticles

For the case of the pinned preradial LC microparticles, we calculated director profiles, van der Waals interaction energies, repulsive electrical double layer energies, and probe colloid fluxes as a function of homeotropic surface anchoring energy and surface potential. Van der Waals interaction energies were evaluated using the numerical integration of Eq. S18 (without shrinking Ω_1). Assuming a LC elastic constant of 6.6 pN, the calculated van der Waals interaction energies for strong (W = 0.66 mN/m) homeotropic anchoring energy are presented in Figure S7A and S7B for probe colloids approaching near the surface defect and near the equator, respectively. Inspection of Figure S7A and S7B reveals that the net interaction energies are non-uniform across the surface of the pinned preradial LC microparticle, with the strongest attractive interactions occurring near the surface defect. We examined predictions of our model using $\psi_{0,1} = \psi_{0,2} = -40$, -50, or -60 mV and, similar to the bipolar LC microparticles, found that a surface potential of -50 mV led to potential energy profile consistent with our experimental observations (for the pinned preradial case, this corresponds to a primary adsorption minimum near the defect but not at the equator). We used the potential energy profiles to calculate colloid fluxes onto the surfaces of the LC microparticles using Eqs. 2 and S20 through S22. Specifically, we calculated the normalized surface densities as a function of homeotropic surface anchoring energy and surface potential (Figure S7C). Inspection of Figure S7C reveals that it was possible to capture our experimentally observed colloid densities on the surfaces of the pinned preradial LC microparticle when the homeotropic anchoring was strong and the surface potential was -50 mV (within experimental confidence intervals, Figure 5). We also examined predictions of our model using a weak (W = 6.6 μN/m) homeotropic anchoring energy (Figure S7C). Interestingly, for the range of surface potentials examined, our model predicted an enhancement of probe colloid density in the vicinity of the surface defect that exceeded the experimentally measured probe colloid density reported in Figure 5.

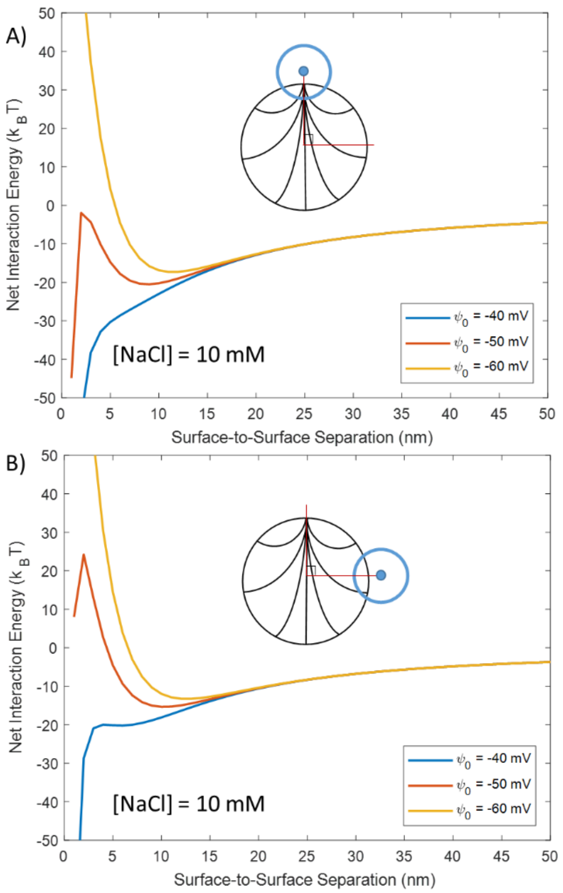

C)

Surface Region	I	II	III	IV	V	VI
Experimental Observation	2.11 ± 0.57	1.23 ± 0.30	1 ± 0.22	1.09 ± 0.22	0.89 ± 0.25	1.16 ± 0.32
W = ψ_0 =						
6.6 µN/m -60 mV	1.66E+22	1.57	1	0.80	0.62	0.58
6.6 µN/m -50 mV	1.97E+13	13.52	1	0.32	0.11	0.05
6.6 µN/m -40 mV	1.13	1.03	1	0.99	0.97	0.97
0.66 mN/m -60 mV	2.19E+2	1.03	1	0.98	0.96	0.96
0.66 mN/m -50 mV	1.98	1.02	1	0.99	0.98	0.98
0.66 mN/m -40 mV	1.00	1.00	1	1.00	1.00	1.00

Figure S7. Application of the theoretical framework to the pinned preradial LC microparticle. Net interaction energies calculated using A_o = 3.2 k_BT, A_m = 0.9 k_BT, *a* = 10 µm, K = 6.6 pN, and probe colloid radius of 0.5 µm for a pinned preradial microparticle with strong (W = 0.66 mN/m) homeotropic anchoring near the surface defect (**A**) and far from the surface defect (**B**). Results are shown for three surface potentials in the presence of 10 mM NaCl (Debye screening length = 3.04 nm). (**C**) Calculated (normalized) surface densities of colloids adsorbed to pinned preradial microparticles, as a function of homeotropic surface anchoring energy and surface potential. The surface densities of colloids adsorbed in each surface region of the microparticle are normalized by the average surface density of adsorbed colloids in a reference region (region III). The surface regions indicated in the table are defined in Figure 5.

LC Microparticles with Polydomains

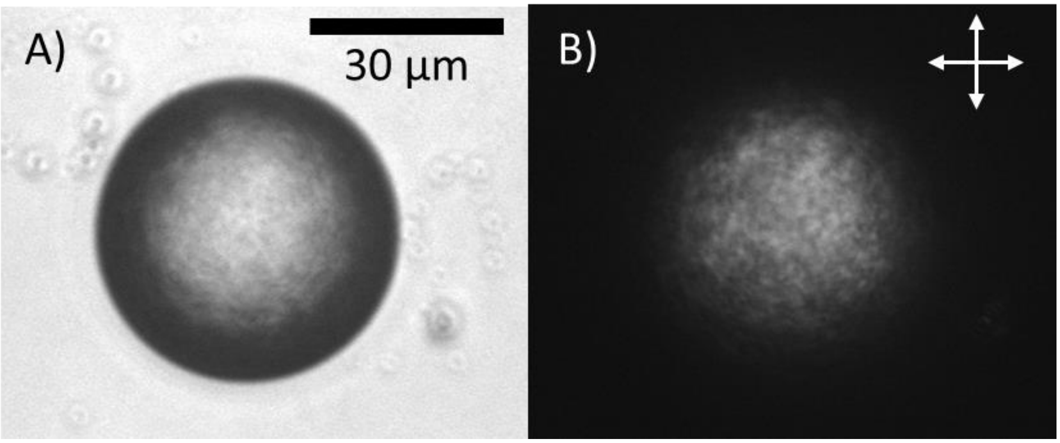

Figure S8. Images of LC microparticle with polydomains. Micrographs of a typical polydomain LC microparticle observed as a by-product during the synthesis of isotropic microparticles. (**A**) Bright field and (**B**) cross-polarized light micrographs of the microparticle.

Predictions of Colloid Flux onto LC Microparticles with Weak Tangential Surface Anchoring or Uniform Configuration

For the case of the bipolar LC microparticle with weak tangential surface anchoring (W = 0.6 μN/m) or the uniform LC microparticle (W = 6.6 nN/m), we calculated director profiles, van der Waals interaction energies, repulsive electrical double layer energies, and probe colloid fluxes at an assumed elastic constant (6.6 pN) and surface potential (-50 mV). Van der Waals interaction energies were evaluated using the numerical integration of Eq. S19 (with shrinking Ω_1). We used the potential energy profiles to calculate colloid fluxes onto the surfaces of the LC microparticles using Eqs. 2 and S20 through S22 (Figure S9). Inspection of Figure S9 reveals that for both sets of LC microparticles, there is an enhancement of predicted normalized surface density in equatorial surface regions (Regions III and IV) compared to our predictions of adsorbed colloid density for bipolar LC microparticles with stronger tangential surface anchoring (Figure 1G). We interpret this result in conjunction with Figure 3F and 4C to indicate that the change in van der Waals attraction energy is more localized to the surface regions near the equator of these LC microparticles. Future works could attempt to analyze the adsorption of probe colloids onto these LC microparticles provided experimental difficulties in obtaining these spheres are overcome (32).

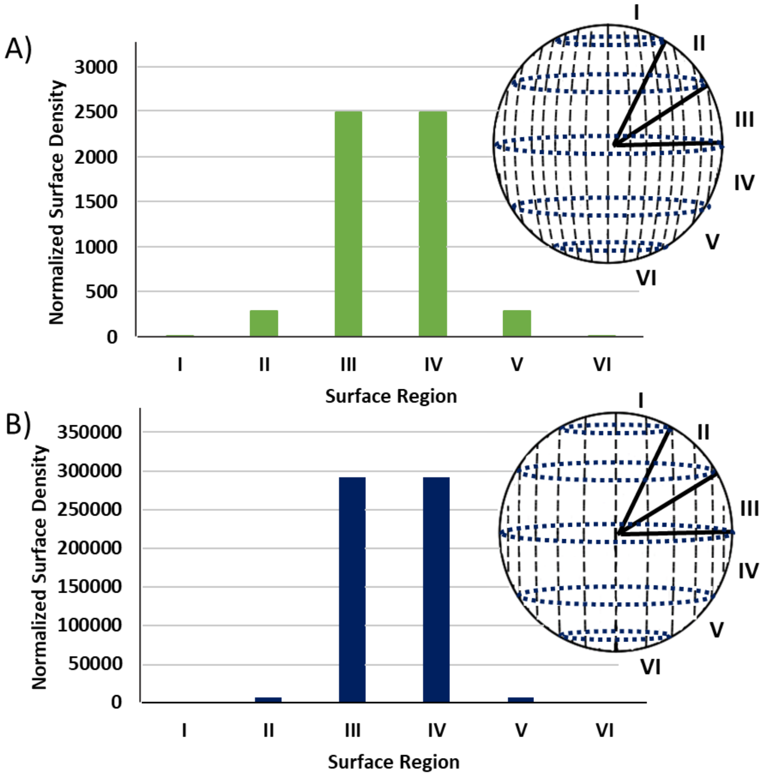

Figure S9. Predicted probe colloid surface distributions on weakly bipolar and uniform LC microparticles. Theoretically predicted, normalized probe PS colloid adsorption density for a weakly bipolar (**A**) and uniform (**B**) liquid crystal microparticle (W = 0.6 µN/m and 6.6 nN/m, respectively) in 10 mM aqueous NaCl. Insets, illustration of the internal ordering of the corresponding LC microparticle and classification of the surface regions. Surface density is normalized to surface region I. Note that adsorption in surface regions I and VI is the value one (not zero) for these LC microparticles.

Discussion of Flexoelectric Effects

Below we discuss the effects of salts on flexoelectric effects, although similar arguments apply for order electric and surface polarization effects. As described by Lavrentovich (*32*), the presence of mobile charges in a LC can screen the flexoelectric polarization. For a LC microdroplet, the critical radius, R_C, above which the effective surface charge density generated by flexoelectricity is screened by the mobile charges in a LC is given by the expression, $R_C = \sqrt{6e_1\kappa/\sigma}$, where e_1 is the flexoelectric coefficient associated with splay, κ is the charge carrier mobility in LC, and σ is the ionic conductivity of the LC. We calculate R_C for pure 5CB (no added salts) to be ~2.5 µm using values for ionic conductivity that we measured previously ($\sigma = 10^{-8}$S/m (*34*)), and charge carrier mobility ($\kappa = 10^{-10}$ m^2/Vs (*51*) and flexoelectric coefficients ($e_1 = 10^{-11}$ C/m (*52*)) reported elsewhere. However, our experimental system is not pure 5CB, but 5CB microdroplets in water to which 10 mM NaCl is added. As reported previously (*33*, *34*), salts from aqueous solutions partition into 5CB. From this prior work, we estimate that the ionic conductivity of 5CB in contact with 10 mM NaCl to be 5×10^{-8} S/m. This further reduces our estimate of Rc in our experiments to $R_C \sim 1$ µm. Importantly, these values of Rc are orders of magnitude smaller than the sizes of the LC microdroplets used in our experiments (20 µm to 80 µm), leading us to conclude that the effects of flexoelectricity are small in our experiments. Flexoelectric effects may become important in systems with lower mobile ion concentrations or with smaller LC microparticles.

REFERENCES AND NOTES

1. J. N. Israelachvili, *Intermolecular and Surface Force* (Academic Press, 2011).

2. S. C. Glotzer, M. J. Solomon, Anisotropy of building blocks and their assembly into complex structures. *Nat. Mater.* **6**, 557–562 (2007).

3. J. C. Loudet, A. M. Alsayed, J. Zhang, A. G. Yodh, Capillary interactions between anisotropic colloidal particles. *Phys. Rev. Lett.* **94**, 018301 (2005).

4. I. B. Liu, N. Sharifi-Mood, K. J. Stebe, Capillary assembly of colloids: Interactions on planar and curved interfaces. *Annu. Rev. Condens. Matter Phys.* **9**, 283–305 (2018).

5. Z. Zhang, Z. Tang, N. A. Kotov, S. C. Glotzer, Simulations and analysis of self-assembly of CdTe nanoparticles into wires and sheets. *Nano Lett.* **7**, 1670–1675 (2007).

6. M. R. Jones, R. J. Macfarlane, A. E. Prigodich, P. C. Patel, C. A. Mirkin, Nanoparticle shape anisotropy dictates the collective behavior of surface-bound ligands. *J. Am. Chem. Soc.* **133**, 18865–18869 (2011).

7. C. R. Iacovella, A. S. Keys, S. C. Glotzer, Self-assembly of soft-matter quasicrystals and their approximants. *Proc. Natl. Acad. Sci. U.S.A.* **108**, 20935–20940 (2011).

8. T. Ding, K. Song, K. Clays, C.-H. Tung, Fabrication of 3D photonic crystals of ellipsoids: Convective self-assembly in magnetic field. *Adv. Mater.* **21**, 1936–1940 (2009).

9. J. D. Forster, J.-G. Park, M. Mittal, H. Noh, C. F. Schreck, C. S. O’Hern, H. Cao, E. M. Furst, E. R. Dufresne, Assembly of optical-scale dumbbells into dense photonic crystals. *ACS Nano* **5**, 6695–6700 (2011).

10. B. D. Smith, K. A. Fichthorn, D. J. Kirby, L. M. Quimby, D. A. Triplett, P. González, D. Hernández, C. D. Keating, Asymmetric van der Waals forces drive orientation of compositionally anisotropic nanocylinders within smectic arrays: Experiment and simulation. *ACS Nano* **8**, 657–670 (2014).

11. N. D. Browning, J. Yuan, L. M. Brown, Theoretical determination of angularly-integrated energy loss functions for anisotropic materials. *Philos. Mag. A* **67**, 261–271 (1993).

12. V. A. Parsegian, G. H. Weiss, Dielectric anisotropy and the van der Waals interaction between bulk media. *J. Adhesion* **3**, 259–267 (1972).

13. P. De Gennes, J. Prost, *The Physics of Liquid Crystals* (Oxford Univ. Press, 1995).

14. M. Nishikawa, B. Taheri, J. L. West, Mechanism of unidirectional liquid-crystal alignment on polyimides with linearly polarized ultraviolet light exposure. *Appl. Phys. Lett.* **72**, 2403–2405 (1998).

15. E. R. Smith, B. W. Ninham, Response of nematic liquid crystals to van der Waals forces. *Phys. Ther.* **66**, 111–130 (1973).

16. E. Dubois-Violette, P. G. De Gennes, Effects of long range van der Waals forces on the anchoring of a nematic fluid at an interface. *J. Colloid Interf. Sci*. **57**, 403–410 (1976).

17. P. C. Mushenheim, N. L. Abbott, Hierarchical organization in liquid crystal-in-liquid crystal emulsions. *Soft Matter* **10**, 8627–8634 (2014).

18. L. Cademartiri, K. J. M. Bishop, Programmable self-assembly. *Nat. Mater.* **14**, 2–9 (2015).

19. M. Kleman, O. D. Lavrentovich, *Soft Matter Physics: An Introduction* (Springer, 2003).

20. P. S. Drzaic, *Liquid Crystal Dispersions* (World Scientific Publishing Company, 1995).

21. O. D. Lavrentovich, Topological defects in dispersed words and worlds around liquid crystals, or liquid crystal drops. *Liq. Cryst.* **24**, 117–126 (1998).

22. D. J. Broer, G. N. Mol, G. Challa, In-situ photopolymerization of oriented liquid-crystalline acrylates, 5. Influence of the alkylene spacer on the properties of the mesogenic monomers and the formation and properties of oriented polymer networks. *Macromol. Chem.* **192**, 59–74 (1991).

23. F. Mondiot, X. Wang, J. J. de Pablo, N. L. Abbott, Liquid crystal-based emulsions for synthesis of spherical and non-spherical particles with chemical patches. *J. Am. Chem. Soc.* **135**, 9972–9975 (2013).

24. D. S. Miller, X. Wang, N. L. Abbott, Design of functional materials based on liquid crystalline droplets. *Chem. Mater.* **26**, 496–506 (2014).

25. R. Hogg, T. W. Healy, D. W. Fuerstenau, Mutual coagulation of colloidal dispersions. *Trans. Faraday Soc.* **62**, 1638–1651 (1966).

26. J. E. Sader, S. L. Carnie, D. Y. C. Chan, Accurate analytic formulas for the double-layer interaction between spheres. *J. Colloid Interf. Sci.* **171**, 46–54 (1995).

27. C. A. Silvera Batista, R. G. Larson, N. A. Kotov, Nonadditivity of nanoparticle interactions. *Science* **350**, 1242477 (2015).

28. L. A. Spielman, Viscous interactions in brownian coagulation. *J. Colloid Interf. Sci.* **33**, 562–571 (1970).

29. M. K. Alam, The effect of van der Waals and viscous forces on aerosol coagulation. *Aerosol Sci. Tech.* **6**, 41–52 (1987).

30. M. A. Gharbi, M. Nobili, C. Blanc, Use of topological defects as templates to direct assembly of colloidal particles at nematic interfaces. *J. Colloid Interf. Sci.* **417**, 250–255 (2014).

31. R. B. Meyer, Piezoelectric effects in liquid crystals. *Phys. Rev. Lett.* **22**, 918–921 (1969).

32. O. D. Lavrentovich, Flexoelectricity of droplets of a nematic liquid crystal. *Pis'ma Zh. Tekh. Fiz.* **14**, 166–171 (1988).

33. R. J. Carlton, J. K. Gupta, C. L. Swift, N. L. Abbott, Influence of simple electrolytes on the orientational ordering of thermotropic liquid crystals at aqueous interfaces. *Langmuir* **28**, 31–36 (2011).

34. R. R. Shah, N. L. Abbott, Coupling of the orientations of liquid crystals to electrical double layers formed by the dissociation of surface-immobilized salts. *J. Phys. Chem. B* **105**, 4936–4950 (2001).

35. G. P. Sinha, F. M. Aliev, Dielectric spectroscopy of liquid crystals in smectic, nematic, and isotropic phases confined in random porous media. *Phys. Rev. E* **58**, 2001–2010 (1998).

36. D. K. Yoon, R. Deb, D. Chen, E. Körblova, R. Shao, K. Ishikawa, N. V. S. Rao, D. M. Walba, I. I. Smalyukh, N. A. Clark, Organization of the polarization splay modulated smectic liquid crystal phase by topographic confinement. *Proc. Natl. Acad. Sci. U.S.A.* **107**, 21311–21315 (2010).

37. J. M. Brake, M. K. Daschner, Y.-Y. Luk, N. L. Abbott, Biomolecular interactions at phospholipid-decorated surfaces of liquid crystals. *Science* **302**, 2094–2097 (2003).

38. G. P. Crawford, D. W. Allender, J. W. Doane, Surface elastic and molecular-anchoring properties of nematic liquid crystals confined to cylindrical cavities. *Phys. Rev. A* **45**, 8963 (1992).

39. Y.-K. Kim, X. Wang, P. Mondkar, E. Bukusoglu, N. L. Abbott, Self-reporting and self-regulating liquid crystals. *Nature* **557**, 539–544 (2018).

40. P. Guillamat, J. Ignés-Mullol, F. Sagués, Control of active liquid crystals with a magnetic field. *Proc. Natl. Acad. Sci. U.S.A.* **113**, 5498–5502 (2016).

41. P. C. Hiemenz, R. Rajagopalan, *Principles of Colloid and Surface Chemistry* (Marcel Deker, 1997).

42. R. G. Horn, Refractive indices and order parameters of two liquid crystals. *J. Phys.* **39**, 105–109 (1978).

43. B. R. Ratna, R. Shashidhar, Dielectric studies on liquid crystals of strong positive dielectric anisotropy. *Mol. Cryst. Liq. Cryst.* **42**, 113–125 (1977).

44. J.-H. Lee, J. J. Lee, Y. J. Lim, S. Kundu, S.-W. Kang, S. H. Lee, Enhanced contrast ratio and viewing angle of polymer-stabilized liquid crystal via refractive index matching between liquid crystal and polymer network. *Opt. Express* **21**, 26914–26920 (2013).

45. P. A. Kossyrev, G. P. Crawford, Yarn ball polymer microstructures: A structural transition phenomenon induced by an electric field. *Appl. Phys. Lett.* **77**, 3752 (2000).

46. A. Rapini, M. Papoular, Distorsion d'une lamelle nématique sous champ magnétique conditions d'ancrage aux parois. *J. Phys. Colloq.* **30**, C4-54–C4-56 (1969).

47. H. C. Hamaker, The London—Van der Waals attraction between spherical particles. *Phys. Ther.* **4**, 1058–1072 (1937).

48. R. J. Hunter, *Foundations of Colloid Science* (Oxford Univ. Press, 2001).

49. R. J. Hunter, *Zeta Potential in Colloid Science: Principles and Applications* (Academic Press, 1981).

50. K. G. Marinova, R. G. Alargova, N. D. Denkov, O. D. Velev, D. N. Petsev, I. B. Ivanov, R. P. Borwankar, Charging of oil-water interfaces due to spontaneous adsorption of hydroxyl ions. *Langmuir* **12**, 2045–2051 (1996).

51. S. Naemura, A. Sawada, Ionic conduction in nematic and smectic a liquid crystals. *Mol. Cryst. Liq. Cryst.* **400**, 79–96 (2003).

52. I. Dozov, P. Martinot-Lagarde, G. Durand, Flexoelectrically controlled twist of texture in a nematic liquid crystal. *J. Phys. Lett.* **43**, 365–369 (1982).